INORGANIC CHEMISTRY
FRONTIERS

RESEARCH ARTICLE

View Article Online
View Journal | View Issue

Cite this: *Inorg. Chem. Front.*, 2023, **10**, 3375

Engineering a non-noble plasmonic center in MOF-derived Z-scheme heterojunctions for enhanced photoelectrochemical water splitting†

Chuanping Li, *[a,b] Tianxiang Hang,[a] Hui Zhou,[a] Ping Ge,[a] Shuoren Li[a] and Xian-Dong Zhu *[a]

Photoelectrochemical (PEC) water splitting is a promising strategy to convert solar power into clean hydrogen energy. However, the poor bulk charge-separation ability and sluggish oxygen evolution dynamics of the photoanodes severely limit the PEC catalytic performance. Herein, a plasmonic perovskite oxide (reduced $SrTiO_3$, R-STO) is synthesized *via* the *in situ* derivation of Ti-metal–organic frameworks (NH_2-MIL-125) and further oxygen-vacancy engineering. Finite-difference time-domain (FDTD) and density functional theory (DFT) calculations forcefully evidence the metallic properties and plasmonic characteristics of the MOF-derived R-STO. Then, a plasmon-promoted direct Z-scheme photoanode (TiO_2@NH_2-MIL-125@R-STO) is designed, which exhibits high PEC water oxidation performance due to the synergistic effect of the MOF-based Z-scheme arrangement and the surface plasmon resonance (SPR) of the non-noble R-STO. This work proposes a new method for the design of high-efficiency PEC nanomaterials.

Received 14th March 2023,
Accepted 27th April 2023

DOI: 10.1039/d3qi00472d

rsc.li/frontiers-inorganic

1 Introduction

Photoelectrochemical (PEC) water splitting is regarded as a promising approach to solve the growing energy crisis and convert abundant solar light into hydrogen energy.[1–4] However, the sluggish evolution of oxygen and expensive hydrogen production costs, recognized as severe constraints for water splitting, increase the demand for the development of economical and stable photoanodes with high-efficiency water oxidation performance.[5–7] For excellent photoanodes, wide absorption range, strong redox ability, high catalytic efficiency, and long-term stability are the key features. Nevertheless, it is rather difficult for a single semiconductor to possess all these properties simultaneously.[8–12]

The fabrication of plasmonic metal–semiconductor heterostructures is an emerging strategy to markedly enhance the photoelectrochemical catalytic performance of semiconductors, which has been proposed to involve either plasmon-induced electromagnetic field enhancement and photothermal conversion or "hot" electron (hole) transfer between plasmonic metals and semiconductors.[13–17] However, the most widely used plasmonic elements are noble metals (Au or Ag), which seriously restricts their practical applications.[18–20] Recently, heavily doped semiconductors (*e.g.* transition metal oxides or transparent conducting oxides) have been found to exhibit a plasmonic effect arising from the high density of free carriers.[21–23]As alternatives to conventional plasmonic noble metals, the plasmonic characteristics of the heavily doped semiconductors can be regulated by controlling the concentration of the free charge carriers in the crystal lattice, which can be achieved by heavily doping lattice vacancies or aliovalent heteroatoms. In recent years, perovskite oxides have been extensively investigated as semiconductors owing to their high stability, favorable light absorption capability, and the flexible controllability of the energy bandgaps.[24,25] Reasonable defect engineering (*e.g.* oxygen vacancies) in the perovskite oxides is expected to be a feasible way to change the local charge density near the defect sites and yield sufficient delocalized electrons to support the plasmon resonance due to the induced intrinsic defects and synchronously massive electrons in the given host structures without extensive structural expansion.[21] However, few investigations have been reported on the SPR effect of perovskite oxides, and the synthesis of novel non-noble plasmonic metals still faces great challenges.

Recently, the fabrication of Z-scheme heterostructures has also been considered an attractive strategy to overcome the

[a]*Anhui Laboratory of Functional Coordinated Complexes for Materials Chemistry and Application, School of Chemical and Environmental Engineering, Anhui Polytechnic University, Wuhu 241000, P. R. China. E-mail: licp@ahpu.edu.cn*
[b]*State Key Laboratory of Electroanalytical Chemistry, Changchun Institute of Applied Chemistry, Chinese Academy of Sciences, 5625 Renmin Street, Changchun 130022, P. R. China*

† Electronic supplementary information (ESI) available. See DOI: https://doi.org/10.1039/d3qi00472d

shortcomings of a single semiconductor.[26–29] For a direct Z-scheme system, the photoexcited electrons with weak reduction capability of semiconductor I will recombine with holes (semiconductor II) of inferior oxidation ability. Correspondingly, the electrons or holes accompanied by strong redox ability will be well preserved. Besides, due to the bandgap difference and built-in electric field between the two semiconductors, the Z-scheme heterostructure can not only extend the light-harvesting range but also improve the electron–hole separation efficiency.[29,30] Metal–organic frameworks (MOFs) have recently emerged as a promising type of photo (electro)catalytic material owing to their semiconductor-like characteristics and abundant structural designability.[31–35] However, the MOF-based Z-scheme heterostructures have been rarely reported due to the rigorous requirements of the electronic band structures between the two semiconductors and challenging difficulties in the efficient coupling of different semiconductors.

Considering the approaches and bottlenecks mentioned above, herein, a plasmonic perovskite oxide-enhanced direct Z-scheme catalyst (TiO_2@NH_2-MIL-125@R-STO) was constructed by the *in situ* derivation of NH_2-MIL-125 and further oxygen-vacancy engineering. The density functional theory (DFT) calculations demonstrated that the R-STO catalyst showed a fundamental transition from semiconductor to plasmonic metal, and the charge density around titanium atoms was much higher than that without oxygen vacancies. Finite-difference time-domain (FDTD) simulations confirmed the SPR effect of R-STO, which effectively accelerated the electron–hole (e–h) separation and decreased the carrier recombination through an internally stronger electromagnetic field. The plasmon-enhanced Z-scheme catalyst (TiO_2@NH_2-MIL-125@R-STO) exhibited a dramatically improved water-splitting performance (~4.4 mA cm^{-2} at 1.23 V *vs.* RHE) in comparison with pristine TiO_2 photoanodes.

2 Experimental section

2.1 Preparation of TiO_2 nanorod arrays

FTO glasses were first washed and dried. The TiO_2 nanorods were grown on the FTO glasses in a typical preparation process. Then, 0.25 mL of TBOT was added to an aqueous HCl solution (15 mL) under vigorous stirring. Subsequently, the precursor solution was transferred into a Teflon autoclave (volume: 50 mL), and two FTO glasses were crisscrossed into the solution. The sealed autoclave was placed in a stable air atmosphere at 150 °C for 4 hours and then TiO_2 NRs were washed with DI water for a few minutes. To obtain the anatase phase, TiO_2 NRs were annealed for 1 h (450 °C).

2.2 Synthesis of TiO_2@NH_2-MIL-125@STO

0.5 mmol of H_2ATA was dissolved in 10 mL of DMF and 0.15 mL of TBOT was dispersed in methanol (10 mL). Afterward, the solutions and TiO_2 NRs/FTO glasses were added to a Teflon autoclave and the sealed autoclave was kept at 150 °C for 10, 20, and 30 hours. Finally, the yellow TiO_2@NH_2-MIL-125 was rinsed with methanol and DMF respectively, and dried for use.

NH_2-MIL-125 was used to replace TiO_2 as the sacrificial template for the *in situ* synthesis of STO. $Sr(OH)_2{\cdot}8H_2O$ (0.02 M) was dissolved in 20 mL of DI water. Then TiO_2@NH_2-MIL-125 was added and transferred to a Teflon autoclave, and heated for 0.5, 1 and 2 hours at 180 °C. Finally, TiO_2@NH_2-MIL-125@STO was obtained after washing with DI water.

2.3 Synthesis of TiO_2@NH_2-MIL-125@R-STO

The obtained TiO_2@NH_2-MIL-125@STO film covered evenly by 0.22 g $NaBH_4$ was annealed at 320 °C for 2 h under an Ar atmosphere. The TiO_2@NH_2-MIL-125@R-STO film was successfully constructed by washing with 0.5 M HCl as well as DI water to wipe off the byproduct.

3 Results and discussion

The plasmonic Z-scheme photoanode (TiO_2@NH_2-MIL-125@R-STO) was prepared by *in situ* MOF derivation and rational defect-engineering. The preparation procedures are illustrated in Fig. 1a. As seen from the SEM images in Fig. 1b,

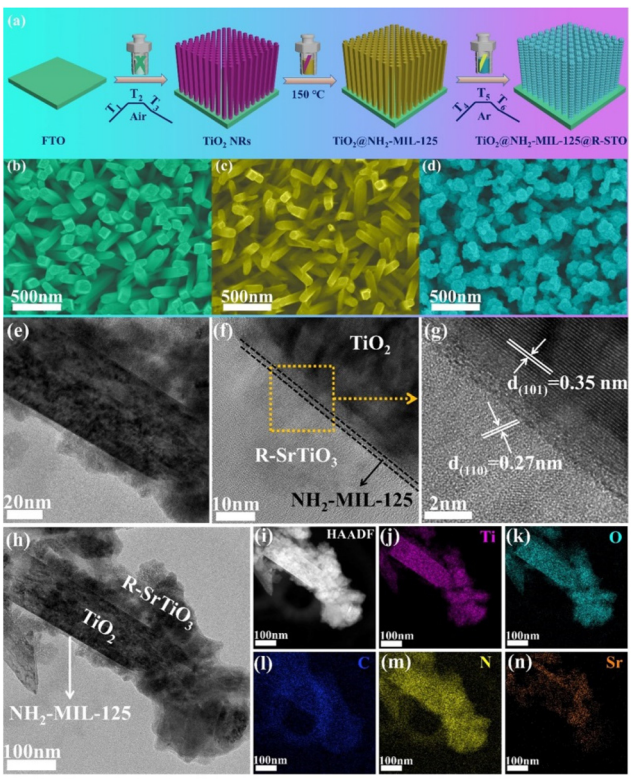

Fig. 1 (a) Synthetic procedure of TiO_2@NH_2-MIL-125@R-STO. SEM images of (b) TiO_2 NRs, (c) TiO_2@NH_2-MIL-125, and (d) TiO_2@NH_2-MIL-125@R-STO. (e–h) TEM images, (i) high angle annular dark-field scanning transmission electron microscopy (HAADF-STEM) image of the TiO_2@NH_2-MIL-125@R-STO, and (j–n) elemental mapping images of Ti, O, C, N, and Sr.

Fig. S1a, and S1d,† TiO_2 NRs were vertically grown on an FTO conducting glass with a side length of about 100 nm and a length of ~1 μm. Then NH_2-MIL-125 was spontaneously coated on TiO_2 NRs using a solvothermal method at 150 °C. Benefiting from the excellent crystal matching between NH_2-MIL-125 and TiO_2, the TiO_2@NH_2-MIL-125 film exhibited a thin overlayer coated on TiO_2 (Fig. 1c, S1b and S1e†). The granular STO was *in situ* derived from NH_2-MIL-125 and further reduced under a hydrogen atmosphere. As displayed in Fig. 1d, Fig. S1c, and S1f,† the morphology of TiO_2@NH_2-MIL-125@R-STO changed significantly compared with TiO_2@NH_2-MIL-125, which is presented with a hierarchical structure in the transmission electron microscopy (TEM) images (Fig. 1e–n). From the HRTEM image in Fig. 1g, the perfect lattice fringes of 0.27 nm and 0.35 nm correspond to the (110) and (101) planes of R-STO and TiO_2, respectively.[36] The EDS elemental mapping images (Fig. 1i–n) clearly reveal the hierarchical distribution of Ti, C, N, O and Sr, further proving the successful fabrication of TiO_2@NH_2-MIL-125@R-STO.

To further investigate and analyze the crystal structures, the powder X-ray diffraction (XRD) patterns were obtained as shown in Fig. 2a. The diffraction peaks of TiO_2@NH_2-MIL-125 in the range of 5–25° were well matched with the characteristic diffraction peaks of NH_2-MIL-125 (CCDC number: 1527308†). After the *in situ* anchoring of STO, three new diffraction peaks existed centering at 32.44°, 40.02°, and 46.54°, which were the characteristic peaks of STO (CCDC number: 900595†), corresponding to the (110), (111), and (200) crystal planes. To confirm the interactions and surface composition of different components, X-ray photoelectron spectroscopy (XPS) measurements were implemented. From Fig. S2,† the full-spectrum scan showed the characteristic peaks of Ti, O, Sr, N and C in the catalyst of TiO_2@NH_2-MIL-125@R-STO, which indicated the successful preparation of heterostructures. As displayed in Fig. 2b, Ti 2p consisted of two peaks situated at 464.28 eV and 458.58 eV, corresponding to Ti $2p_{1/2}$ and Ti $2p_{3/2}$ of the initial TiO_2 NRs.[37] In contrast to TiO_2 NRs, the spectrum of Ti 2p in TiO_2@NH_2-MIL-125 was negatively shifted, suggesting that the surface composition of Ti^{4+} has been subtly changed due to the new formation of NH_2-MIL-125. After the anchoring of STO on TiO_2@NH_2-MIL-125, the peak of Ti 2p and N 1s spectra (Fig. S3†) positively shifted, manifesting the charge transfer between STO and NH_2-MIL-125. As presented in Fig. 2c, the peaks centered at 531.6 and 530.1 eV belong to the oxygen vacancies (O_V) and lattice oxygen (O_L), respectively. The ratio of O_V/O_L could be used to evaluate the density of the O_V.[38] After the high-temperature hydrogen reduction process, the ratio of O_V/O_L increased and the Sr 3d peaks of TiO_2@NH_2-MIL-125@R-STO slightly shifted to lower binding energies due to the differences in chemical environments compared with TiO_2@NH_2-MIL-125@STO (Fig. 2d). All the XPS results confirmed the successful preparation of TiO_2@NH_2-MIL-125@R-STO.

To explore the plasmonic effect of R-STO, theoretical investigations based on DFT calculations were conducted according to the calculation models (Fig. S4†). As shown from the calculated band structure (Fig. 3a and b) and the corresponding density of states (DOS) in Fig. 3c and d, the pristine STO exhibited semiconductor characteristics with discontinuous electronic states at the Fermi level. Meanwhile after the oxygen-vacancy engineering, the R-STO presented a metallic character with substantial electronic states crossing the Fermi level made up of Ti 3d orbitals. Moreover, the free charge distribution diagrams (Fig. 3e and f) indicated that the free electron density around Ti atoms with oxygen vacancies was delocalized and was higher than that of Ti atoms of the pristine STO. Due to the large amount of free electrons introduced by oxygen vacancies, the R-STO was expected to exhibit a strong LSPR effect. This result was supported by the FDTD simulations according to the refractive index of R-STO obtained from the ellipsometer (Fig. S5†). As shown in Fig. 3g, the R-STO exhibited conspicuous electromagnetic (EM) field enhancement under light irradiation. The strong EM field around the R-STO forcefully evidenced the plasmonic effect of R-STO.

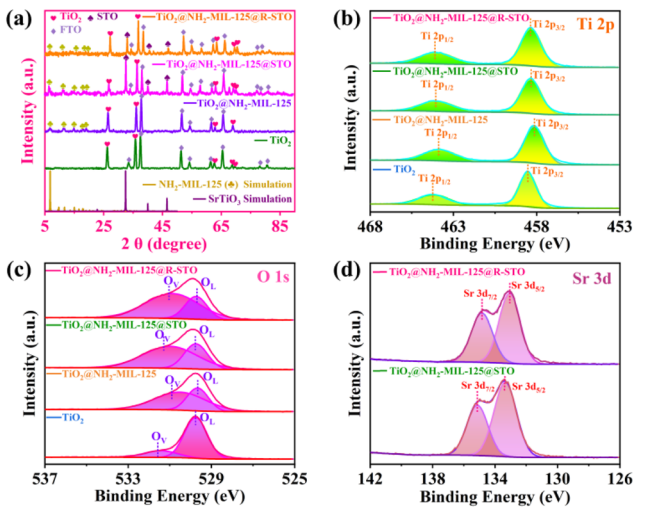

Fig. 2 (a) XRD patterns of the prepared PEC catalysts. XPS survey spectra of (b) Ti 2p, (c) O 1s, and (d) Sr 3d.

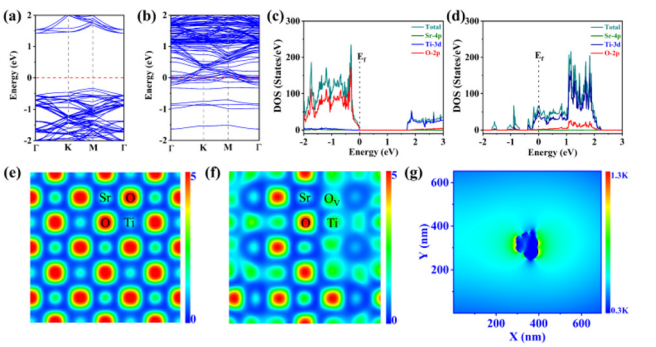

Fig. 3 Band structure of bulk $SrTiO_3$ without (a) and with (b) oxygen vacancy. The DOS of bulk $SrTiO_3$ without (c) and with (d) oxygen vacancy. The charge density distribution of bulk $SrTiO_3$ without oxygen vacancy (e) and with oxygen vacancy (f). (g) Spatial electromagnetic field distribution of R-STO.

To further identify the plasmonic Z-scheme configuration of TiO_2@NH_2-MIL-125@R-STO, the electronic band structures and charge transfer pathways were elaborately investigated. As seen from the valence band XPS (VB-XPS) in Fig. 4a and b, the position of the VB of NH_2-MIL-125 and TiO_2 could be estimated to be 2.55 eV and 2.25 eV, respectively. Fig. 4c and S6† show the Tauc plots of TiO_2 and NH_2-MIL-125. According to the results, the bandgaps were calculated to be 2.80 and 2.35 eV for TiO_2 and NH_2-MIL-125. According to the equation $E_c = E_v - E_g$, the energies of the conduction band (E_c) of TiO_2 and NH_2-MIL-125 were −0.55 and 0.20 eV, respectively. Such a band alignment was expected to be favorable for the preparation of the Z-scheme configuration.[29] To confirm this prediction, electron paramagnetic resonance (EPR) spectroscopy was conducted to investigate the electron transfer pathway during the PEC catalytic process. As shown in Fig. 4d and e, since the conduction band (CB) was not negative enough, the reduction ability of NH_2-MIL-125 was too weak to reduce O_2 to O_2^-, and only the DMPO-OH signal was observed in NH_2-MIL-125. In comparison, both the DMPO-OH and the DMPO-O_2^- signals were traced in TiO_2@NH_2-MIL-125 and TiO_2, which validated the Z-scheme configuration of the sample as expected. Upon light irradiation, the photo-excited electrons of NH_2-MIL-125 would be recombined with the holes of TiO_2. Meanwhile, the electrons of TiO_2 and the holes of NH_2-MIL-125 with stronger redox capability would be preserved, exposing improved charge carrier separation and participating in the subsequent catalytic process (Fig. 4f). To further prove the plasmonic effect and confirm the space-resolved electromagnetic field enhancement of R-STO in the TiO_2@NH_2-MIL-125@R-STO heterostructures, FDTD simulation was conducted as shown in Fig. 5a and b. In comparison with TiO_2@NH_2-MIL-125, the intensity of the spatial electromagnetic (EM) field at the interface of NH_2-MIL-125 and TiO_2 was obviously enhanced owing to the SPR effect of R-STO. Such an enhanced EM field and simultaneous nonradiative hot electrons have been proved to improve the electron–hole separation efficiency and finally increase the number of charge carriers involved in the catalytic

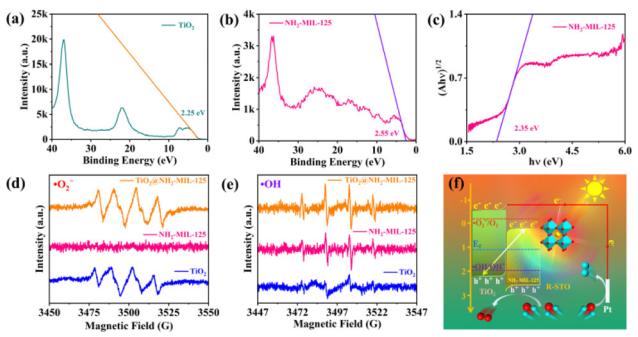

Fig. 4 The VB-XPS of (a) TiO_2 and (b) NH_2-MIL-125, (c) the Tauc plot of NH_2-MIL-125. EPR spectra of (d) DMPO-O_2^-, (e) DMPO-OH for TiO_2, NH_2-MIL-125, and TiO_2@NH_2-MIL-125. (f) A schematic diagram of the energy band position and photo-excited electron–hole transfer pathways of TiO_2@NH_2-MIL-125@R-STO.

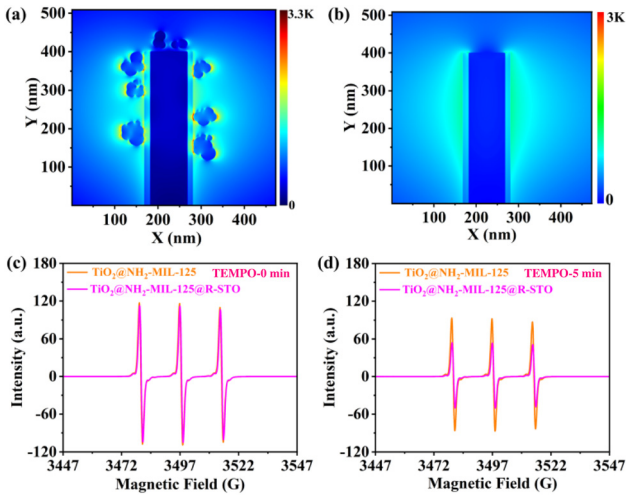

Fig. 5 The EM field distribution of (a) TiO_2@NH_2-MIL-125@R-STO and (b) TiO_2@NH_2-MIL-125. EPR spectra of h^+ signal results of TiO_2@NH_2-MIL-125 and TiO_2@NH_2-MIL-125@R-STO at different times: (c) 0 min and (d) 5 min.

reactions.[39,40] 2,2,6,6-Tetramethyl-1-piperidinyloxy (TEMPO) is a signal molecule used for monitoring the quantity of free h^+ as a radical scavenger of holes. In the presence of the photo-excited holes, the TEMPO would be consumed and thus result in the decrease of the EPR signal. As displayed in Fig. 5c and d, after being irradiated with simulated sunlight, the EPR signal of TEMPO in TiO_2@NH_2-MIL-125@R-STO decreased much more than that in TiO_2@NH_2-MIL-125, suggesting the improved electron–hole separation derived from the strong EM field enhancement and nonradiative hot electron injection. This result was consistent with the FDTD simulations and verified the improvement of the plasmonic Z-scheme configuration (TiO_2@NH_2-MIL-125@STO).

The PEC water oxidation performance was systematically investigated in a three-electrode system by the current density *versus* potential (*J*–*V*) curves in a 0.5 M Na_2SO_4 aqueous solution. The optimal thickness of NH_2-MIL-125 was investigated according to the PEC performance shown in Fig. S7 and S8.† With an increase in the hydrothermal time, the overgrowth of NH_2-MIL-125 could result in reduced catalytic performance due to the poor electrical conductivity of NH_2-MIL-125, which led to more charge recombination and finally reduced PEC performance. Moreover, we also explored the optimal derivation time of STO, and the photocurrent density reached a peak value when the derivation time was 1 h (Fig. S9 and S10†). As displayed in Fig. 6a, S11 and S12,† TiO_2@NH_2-MIL-125@R-STO displayed a remarkably enhanced photocurrent density (~4.4 mA cm^{-2} at 1.23 V *vs.* RHE), which was three times larger than that of pristine TiO_2. Moreover, compared with the recently reported photoanodes in Table S1,† the photocurrent density of TiO_2@NH_2-MIL-125@R-STO was much higher than or comparable with those reported previously. In addition, according to eqn S1,† the plasmonic TiO_2@NH_2-MIL-125@R-STO exhibited an applied bias photon-

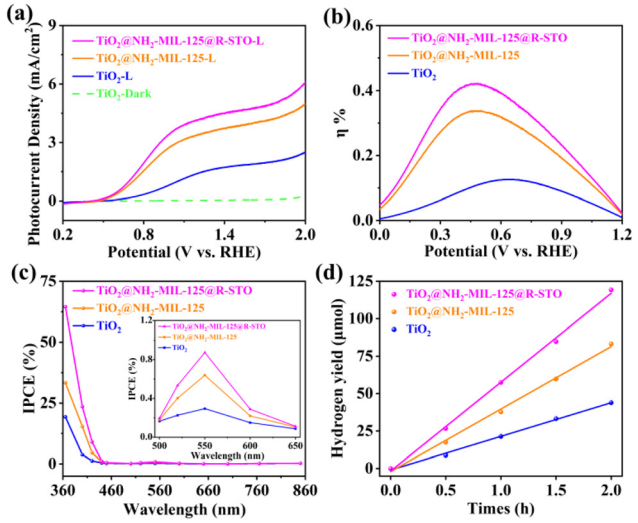

Fig. 6 (a) LSV curves, (b) the ABPE and (c) IPCE values of the as-prepared samples. (d) The amount of H_2 produced by the as-prepared photoanodes at 1.23 V under AM 1.5 G illumination.

to-current efficiency (ABPE) of 0.42% at 0.5 V, which was much higher than those of pristine TiO_2 (0.12% at 0.64 V) and TiO_2@NH_2-MIL-125 (0.33% at 0.5 V) (Fig. 6b). As shown in Fig. S13,† EIS was performed to further investigate the kinetics of the PEC water oxidation. From the Nyquist plots, TiO_2@NH_2-MIL-125@R-STO had a much smaller charge transfer resistance than TiO_2@NH_2-MIL-125 and pristine TiO_2, confirming the faster charge transfer rate and water oxidation kinetics of TiO_2@NH_2-MIL-125@R-STO. To obtain the solar energy conversion efficiency of the catalysts, the incident photon-to-electron conversion efficiency (IPCE) was evaluated according to the following eqn (1):

$$\mathrm{IPCE} = \frac{1240 \times J}{\lambda \times P} \times 100\% \quad (1)$$

where J is the photocurrent density (mA cm^{-2}), λ is the wavelength of the monochromatic light (nm), and P is the light intensity (mW cm^{-2}).[41] As displayed in Fig. 6c, the IPCE value of TiO_2@NH_2-MIL-125 was much higher due to the excellent light-harvesting ability and improved charge separation originating from the Z-scheme configuration. This result is consistent with the UV-visible absorption spectra shown in Fig. S14.† Moreover, the IPCE value of TiO_2@NH_2-MIL-125@R-STO further increased to 65% at 365 nm, proving the highly efficient light scattering/trapping ability of the plasmonic R-STO. Fig. 6d shows the hydrogen production rates for the photoelectrodes under AM 1.5 irradiation. The actual production rates of the samples were evaluated with a homemade reaction cell system (a schematic diagram is shown in Fig. S15 and S16†). The production rate of TiO_2 nanorod arrays was about 21.3 μmol h^{-1} cm^{-2}. After the formation of the Z-scheme system, this value increased to 37.7 μmol h^{-1} cm^{-2}. Remarkably, the H_2 generation rate of TiO_2@NH_2-MIL-125@R-STO further increased to 58.5 μmol h^{-1} cm^{-2}, which was about 2.7-fold higher than that of pristine TiO_2 (Movie S1†). From the stability test shown in Fig. S17a,† TiO_2@NH_2-MIL-125@R-STO exhibited excellent stability without a visible decrease. Moreover, the structure of the catalyst remained intact as identified by the XRD test (Fig. S17b†). All the results presented confirmed that the plasmonic TiO_2@NH_2-MIL-125@R-STO possessed an excellent PEC water oxygen ability as expected.

To further explore the deep mechanisms beyond the superior PEC performance of TiO_2@NH_2-MIL-125@R-STO, the charge carrier behavior was well investigated from thermodynamics and kinetics aspects. First, the carrier density (N_D) was estimated from the Mott–Schottky (M–S) curves (Fig. 7a) using the following formula (2):

$$N_D = \left(\frac{2}{e\varepsilon_r\varepsilon_0}\right)\left[\frac{d(1/C^2)}{dV}\right]^{-1} \quad (2)$$

where ε_r and ε_0 are the permittivity of samples and vacuum, respectively, and C is the capacitance.[41] The N_D values of TiO_2@NH_2-MIL-125 and TiO_2@NH_2-MIL-125@R-STO were calculated to be about 4.9×10^{27} m^{-3} and 1.3×10^{28} m^{-3}, which were much higher than that of pristine TiO_2 (5.6×10^{26} m^{-3}). Furthermore, from the open-circuit voltage–time curves (OCP, Fig. S18†), the OCP value of TiO_2@NH_2-MIL-125@R-STO (~200 mV) and TiO_2@NH_2-MIL-125 (~175 mV) was much larger compared with that of pristine TiO_2 (~150 mV). Fig. S19† shows the Bode-phase curves of the samples. The carrier lifetime (τ_e) could be obtained using the following eqn (3):

$$\tau_e = \frac{1}{2\pi \times f_{max}} \quad (3)$$

where f_{max} is the peak frequency of the Bode-phase plots. It can be seen that the τ_e of TiO_2@NH_2-MIL-125@R-STO (41.6 ms) was much longer than those of TiO_2 (28.3 ms) and

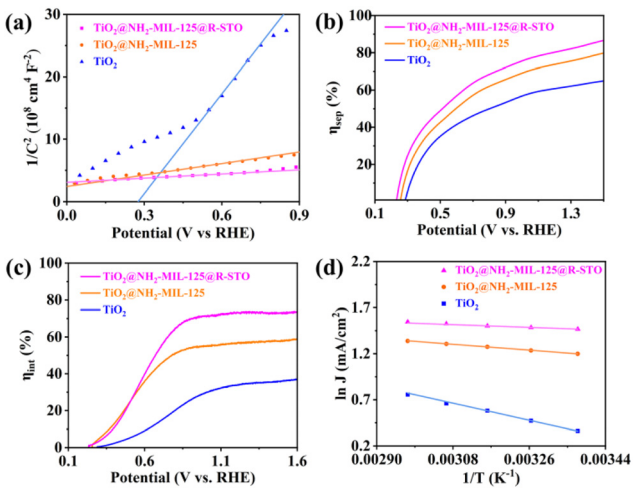

Fig. 7 (a) M–S plots, (b) the charge separation efficiency (η_{sep}), (c) the charge transfer efficiency of the interface/electrode (η_{inj}), and (d) the Arrhenius plots for TiO_2, TiO_2@NH_2-MIL-125, and TiO_2@NH_2-MIL-125@R-STO.

TiO_2@NH_2-MIL-125 (34.3 ms). The prolonged electron lifetime indicated a faster charge transfer rate owing to the collaborative coupling of the heterostructure and the plasmonic effect of R-STO. Fig. 7b shows the charge separation efficiency (η_{sep}) estimated by dividing $J_{sulfite}$ by J_{abs}, where J_{abs} is calculated from the standard AM 1.5G solar spectrum (eqn S2†) and $J_{sulfite}$ is the photocurrent density in 0.5 M Na_2SO_3/Na_2SO_4 (Fig. S20†). The η_{sep} of pristine TiO_2 was 61.2% at 1.23 V *vs.* RHE, while after the coating of NH_2-MIL-125, η_{sep} increased to 73.8% due to the formation of the Z-scheme heterostructure. Upon the introduction of plasmonic R-STO, the charge separation efficiency was further improved, reaching 79.8%. This could be ascribed to the ingenious *in situ* derivation of interface structure design and the EM field enhancement and hot electron injection of the plasmonic R-STO, which resulted in suppression of the bulk carrier recombination and promotion of the charge separation efficiency of the photoanode. The surface carrier injection (η_{inj}) was also calculated to investigate the proportion of holes involved in water oxidation using the following equation: $\eta_{inj} = J_{water}/J_{sulfite}$, where J_{water} is the photocurrent density measured in 0.5 M Na_2SO_4 (Fig. 7c). TiO_2 showed a η_{inj} of 34.3% at 1.23 V (*vs.* RHE), while for TiO_2@NH_2-MIL-125@R-STO, the surface injection efficiency increased to 72.6%. The improved carrier injection was attributed to the promotion of OER dynamics and enlarged specific area of the plasmonic Z-scheme configuration. To estimate the energy barriers and thermodynamic behavior of the reaction, the Arrhenius plots under simulated solar light irradiation were drawn. From Fig. 7d, the activation energy (E_a) could be calculated to be 1.376, 2.954 and 8.549 kJ mol^{-1} for TiO_2@NH_2-MIL-125@R-STO, TiO_2@NH_2-MIL-125 and TiO_2. This result was consistent with the PEC catalytic performance, and the reaction barrier of the PEC water oxidation was decreased by the cooperative coupling effect of TiO_2@NH_2-MIL-125 and plasmonic R-STO, thus finally contributing to the fast reaction kinetics.

4 Conclusions

In summary, a plasmonic R-STO-enhanced direct Z-scheme catalyst, name TiO_2@NH_2-MIL-125@R-STO, was prepared by the *in situ* derivation of NH_2-MIL-125 and oxygen-vacancy engineering. The DFT calculations and FDTD simulations revealed the metallic character and plasmonic property of R-STO, which significantly improved the PEC catalytic activity due to the light scattering/trapping, EM field enhancement and hot electron injection processes of plasmonic R-STO. Moreover, the EPR spectra confirmed the Z-scheme arrangement of TiO_2@NH_2-MIL-125. Under the synergetic effects arising from the Z-scheme configuration and plasmonic effect of R-STO, the photocurrent density could be achieved up to 4.4 mA cm^{-2} at 1.23 V (*vs.* RHE). The reaction dynamics and thermodynamic mechanism investigations provided further evidence that the plasmonic TiO_2@NH_2-MIL-125@R-STO could result in suppression of the bulk carrier recombination and promotion of the charge separation efficiency, thus finally promoting the PEC water oxidation performance. It is believed that our findings offer a new method for the design of highly efficient PEC photoanodes.

Conflicts of interest

There are no conflicts to declare.

Acknowledgements

This work is financially supported by the National Natural Science Foundation of China (22004002), the Natural Science Foundation of Anhui Province (2008085QB80) and the Outstanding Youth Talents Fund of Higher Education of Anhui (2022AH030100). The authors also thank Lei He from Shiyanjia Lab (**https://www.shiyanjia.com**) for the EPR measurements.

References

1 H. Tada, T. Mitsui, T. Kiyonaga, T. Akita and K. Tanaka, All-solid-state Z-scheme in CdS–Au–TiO_2 three-component nanojunction system, *Nat. Mater.*, 2006, **5**, 782–786.
2 S. Hu, M. R. Shaner, J. A. Beardslee, M. Lichterman, B. S. Brunschwig and N. S. Lewis, Amorphous TiO_2 coatings stabilize Si, GaAs, and GaP photoanodes for efficient water oxidation, *Science*, 2014, **344**, 1005–1009.
3 P. Zhang, X. F. Lu, D. Luan and X. W. Lou, Fabrication of heterostructured Fe_2TiO_5–TiO_2 nanocages with enhanced photoelectrochemical performance for solar energy conversion, *Angew. Chem., Int. Ed.*, 2020, **59**, 1–6.
4 Z. Q. Wei, S. Hou, S. C. Zhu, Y. Xiao, G. Wu and F. X. Xiao, Polymer-mediated electron tunneling towards solar water oxidation, *Adv. Funct. Mater.*, 2022, **32**, 2106338.
5 X. Zhang, P. Zhai, Y. Zhang, Y. Wu, C. Wang, L. Ran, J. Gao, Z. Li, B. Zhang, Z. Fan, L. Sun and J. Hou, Engineering single-atomic Ni–N4–O sites on semiconductor photoanodes for high-performance photoelectrochemical water splitting, *J. Am. Chem. Soc.*, 2021, **143**, 20657–20669.
6 H. Song, S. Luo, H. Huang, B. Deng and J. Ye, Solar-driven hydrogen production: recent advances, challenges, and future perspectives, *ACS Energy Lett.*, 2022, **7**, 1043–1065.
7 Y. Kuang, Q. Jia, G. Ma, T. Hisatomi, T. Minegishi, H. Nishiyama, M. Nakabayashi, N. Shibata, T. Yamada, A. Kudo and K. Domen, Ultrastable low-bias water splitting photoanodes via photocorrosion inhibition and in situ catalyst regeneration, *Nat. Energy*, 2016, **2**, 1–9.
8 J. B. Pan, B. H. Wang, J. B. Wang, H. Z. Ding, W. Zhou, X. Liu, J. R. Zhang, S. Shen, J. K. Guo and L. Chen, Activity and stability boosting of an oxygen-vacancy-rich $BiVO_4$ photoanode by NiFe-MOFs thin layer for water oxidation, *Angew. Chem., Int. Ed.*, 2021, **133**, 1453–1460.

9 J. M. Yu, J. Lee, Y. S. Kim, J. Song and J. Jang, High-performance and stable photoelectrochemical water splitting cell with organic-photoactive-layer-based photoanode, *Nat. Commun.*, 2020, **11**, 1–9.
10 H. She, P. Yue, X. Ma, J. Huang, L. Wang and Q. Wang, Fabrication of $BiVO_4$ photoanode cocatalyzed with NiCo-layered double hydroxide for enhanced photoactivity of water oxidation, *Appl. Catal., B*, 2020, **263**, 118280.
11 S. Ren, M. Sun, X. Guo, X. Liu, X. Zhang and L. Wang, Interface-confined surface engineering via photoelectrochemical etching toward solar neutral water splitting, *ACS Catal.*, 2022, **12**, 1686–1696.
12 B. Tang, S.-C. Zhu, H. Liang, S. Li, B.-J. Liu and F.-X. Xiao, Tuning atomically precise metal nanocluster mediated photoelectrocatalysis via a non-conjugated polymer, *J. Mater. Chem. A*, 2022, **10**, 4032–4042.
13 J. Zhao, S. Xue, R. Ji, B. Li and J. Li, Localized surface plasmon resonance for enhanced electrocatalysis, *Chem. Soc. Rev.*, 2021, **50**, 12070–12097.
14 Z. Li, Z. Wang, J. Li, Q. Zhu, Z. Wang and Z. Dai, Enhancing photoelectric response of an Au@Ag/AgI Schottky contact through regulation of localized surface plasmon resonance, *J. Am. Chem. Soc.*, 2021, **143**, 13478–13482.
15 Y.-H. Chen, R. R. Tamming, K. Chen, Z. Zhang, F. Liu, Y. Zhang, J. M. Hodgkiss, R. J. Blaikie, B. Ding and M. Qiu, Bandgap control in two-dimensional semiconductors via coherent doping of plasmonic hot electrons, *Nat. Commun.*, 2021, **12**, 4332.
16 S.-S. Wang, L. Jiao, Y. Qian, W.-C. Hu, G.-Y. Xu, C. Wang and H.-L. Jiang, Boosting electrocatalytic hydrogen evolution over metal–organic frameworks by plasmon-induced hot-electron injection, *Angew. Chem., Int. Ed.*, 2019, **58**, 10713–10717.
17 Z. Zeng, T. Li, Y.-B. Li, X.-C. Dai, M.-H. Huang, Y. He, G. Xiao and F.-X. Xiao, Plasmon-induced photoelectrochemical water oxidation enabled by in situ layer-by-layer construction of cascade charge transfer channel in multilayered photoanode, *J. Mater. Chem. A*, 2018, **6**, 24686–24692.
18 M. Sayed, J. Yu, G. Liu and M. Jaroniec, Non-noble plasmonic metal-based photocatalysts, *Chem. Rev.*, 2022, **122**, 10484–10537.
19 L. Mascaretti, A. Dutta, Š. Kment, V. M. Shalaev, A. Boltasseva, R. Zbořil and A. Naldoni, Plasmon-enhanced photoelectrochemical water splitting for efficient renewable energy storage, *Adv. Mater.*, 2019, **31**, 1805513.
20 F. X. Xiao and B. Liu, Plasmon-dictated photo-electrochemical water splitting for solar-to-chemical energy conversion: Current status and future perspectives, *Adv. Mater. Interfaces*, 2018, **5**, 1701098.
21 H. Cheng, M. Wen, X. Ma, Y. Kuwahara, K. Mori, Y. Dai, B. Huang and H. Yamashita, Hydrogen doped metal oxide semiconductors with exceptional and tunable localized surface plasmon resonances, *J. Am. Chem. Soc.*, 2016, **138**, 9316–9324.
22 Y. Kuwahara, Y. Yoshimura, K. Haematsu and H. Yamashita, Mild deoxygenation of sulfoxides over plasmonic molybdenum oxide hybrid with dramatic activity enhancement under visible light, *J. Am. Chem. Soc.*, 2018, **140**, 9203–9210.
23 S. Ishii, S. L. Shinde and T. Nagao, Nonmetallic materials for plasmonic hot carrier excitation, *Adv. Opt. Mater.*, 2019, **7**, 1800603.
24 W. Li, K. Jiang, Z. Li, S. Gong, R. L. Z. Hoye, Z. Hu, Y. Song, C. Tian, J. Kim, K. H. L. Zhang, S. Cho and J. L. MacManus-Driscoll, Origin of improved photoelectrochemical water splitting in mixed perovskite oxides, *Adv. Energy Mater.*, 2018, **8**, 1801972.
25 W. Wang, M. Xu, X. Xu, W. Zhou and Z. Shao, Perovskite oxide based electrodes for high-performance photoelectrochemical water splitting, *Angew. Chem., Int. Ed.*, 2020, **59**, 136–152.
26 J. Li, S. K. Cushing, P. Zheng, T. Senty, F. Meng, A. D. Bristow, A. Manivannan and N. Wu, Solar hydrogen generation by a CdS–Au–TiO_2 sandwich nanorod array enhanced with au nanoparticle as electron relay and plasmonic photosensitizer, *J. Am. Chem. Soc.*, 2014, **136**, 8438–8449.
27 S. Chen, T. Takata and K. Domen, Particulate photocatalysts for overall water splitting, *Nat. Rev. Mater.*, 2017, **2**, 17050.
28 S. Chen, J. J. M. Vequizo, Z. Pan, T. Hisatomi, M. Nakabayashi, L. Lin, Z. Wang, K. Kato, A. Yamakata, N. Shibata, T. Takata, T. Yamada and K. Domen, Surface modifications of $(ZnSe)_{0.5}(CuGa_{2.5}Se_{4.25})_{0.5}$ to promote photocatalytic Z-scheme overall water splitting, *J. Am. Chem. Soc.*, 2021, **143**, 10633–10641.
29 J. Abdul Nasir, A. Munir, N. Ahmad, T. u. Haq, Z. Khan and Z. Rehman, Photocatalytic Z-scheme overall water splitting: Recent advances in theory and experiments, *Adv. Mater.*, 2021, **33**, 2105195.
30 H. J. Li, W. G. Tu, Y. Zhou and Z. G. Zou, Z-Scheme photocatalytic systems for promoting photocatalytic performance: Recent progress and future challenges, *Adv. Sci.*, 2016, **3**, 12.
31 B. He, Q. Zhang, Z. Pan, L. Li, C. Li, Y. Ling, Z. Wang, M. Chen, Z. Wang, Y. Yao, Q. Li, L. Sun, J. Wang and L. Wei, Freestanding metal–organic frameworks and their derivatives: an emerging platform for electrochemical energy storage and conversion, *Chem. Rev.*, 2022, **122**, 10087–10125.
32 J. Lee, O. K. Farha, J. Roberts, K. A. Scheidt, S. T. Nguyen and J. T. Hupp, Metal–organic framework materials as catalysts, *Chem. Soc. Rev.*, 2009, **38**, 1450–1459.
33 J.-D. Xiao and H.-L. Jiang, Metal–organic frameworks for photocatalysis and photothermal catalysis, *Acc. Chem. Res.*, 2019, **52**, 356–366.
34 C. He, Q.-J. Wu, M.-J. Mao, Y.-H. Zou, B.-T. Liu, Y.-B. Huang and R. Cao, Multifunctional gold nanoparticles@imidazolium-based cationic covalent triazine frameworks for efficient tandem reactions, *CCS Chem.*, 2021, **3**, 2368–2380.

35 J. Sun, X. Zhang, D. Zhang, Y.-P. Chen, F. Wang, L. Li, T.-F. Liu, H. Yang, J. Song and R. Cao, Building block symmetry relegation induces mesopore and abundant open-metal sites in metal–organic frameworks for cancer therapy, *CCS Chem.*, 2022, **4**, 996–1006.
36 H. Tan, Z. Zhao, W.-b. Zhu, E. N. Coker, B. Li, M. Zheng, W. Yu, H. Fan and Z. Sun, Oxygen vacancy enhanced photocatalytic activity of Perovskite $SrTiO_3$, *ACS Appl. Mater. Interfaces*, 2014, **6**, 19184–19190.
37 Q. Pan, A. Li, Y. Zhang, Y. Yang and C. Cheng, Rational design of 3D hierarchical ternary $SnO_2/TiO_2/BiVO_4$ arrays photoanode toward efficient photoelectrochemical performance, *Adv. Sci.*, 2020, **7**, 1902235.
38 Y. He, P. Wang, J. Zhu, Y. Yang, Y. Liu, M. Chen, D. Cao and X. Yan, Synergistical dual strategies based on in situ-converted heterojunction and reduction-induced surface oxygen vacancy for enhanced photoelectrochemical performance of TiO_2, *ACS Appl. Mater. Interfaces*, 2019, **11**, 37322–37329.
39 Y. Zhang, W. Guo, Y. Zhang and W. D. Wei, Plasmonic photoelectrochemistry: In view of hot carriers, *Adv. Mater.*, 2021, **33**, 2006654.
40 C. Li and Y. Jin, Shell-isolated plasmonic nanostructures for biosensing, catalysis, and advanced nanoelectronics, *Adv. Funct. Mater.*, 2021, **31**, 2008031.
41 C. Li, S. Li, T. Hang, F. Guo, X.-D. Zhu and T.-F. Liu, Metal–organic frameworks derived plasmonic catalyst with full spectral response for photoelectrochemical water splitting enhancement, *Small Struct.*, 2022, **3**, 2100071.